31ST EUROPEAN ROTORCRAFT FORUM

Session B2-C2 / CFD Complete
Paper 7

Quasi-Steady Simulation of a Complete EC-145 Helicopter:

Fuselage
+ Main / Tail Actuator Discs
+ Engines

F. Le Chuiton
DLR – German Aerospace Center
in the Helmholtz-Association
Institute of Aerodynamics and Flow Technology
Braunschweig – Germany

September 13-15th, 2005
Firenze
Italy

QUASI-STEADY SIMULATION OF A COMPLETE EC-145 HELICOPTER: FUSELAGE + MAIN / TAIL ACTUATOR DISCS + ENGINES

Frédéric Le Chuiton
DLR – German Aerospace Center
in the Helmholtz-Association
Institute of Aerodynamics and Flow Technology

Abstract

As concluding activity for quasi-steady computations of the French-German helicopter programme CHANCE, the simulation of engine plumes using boundary conditions is presented. First, the one-dimensional theory of characteristics is used to derive boundary quantities for the Euler equations and also for their preconditioned version for low-velocities (after Choi & Merkle). A slight adaption of the scalar dissipation is also suggested for strong temperature gradients. Then, after the presentation of the EC-145 helicopter configuration, the results of a demonstration computation are presented and commented on. The engine inlet and outlet areas have reached a stable state and exhibit a relatively complex surface flow pattern. It is shown that the plumes of hot gases experience several stretch and distortion phases as they convect downstream from the engine nozzle down to aft the horizontal stabilisers. Also the influence of the downwash of both actuator discs is evidenced in showing how the separation bubble is shifted to the left and how the plume of exhaust gases deforms, thus resulting in only one hot spot on the left horizontal stabiliser instead of one on each side. The pressure distribution on the top centre-line experiences only minor modifications at engine inlet and outlet, whereas the temperature distribution increases along the tail boom. Finally, it is shown that the presence of hot gases impinging on the horizontal stabilisers may reduce the magnitude of the negative lift.

Nomenclature

Latin characters:

$\mathcal{A}$	contracted Jacobian matrix
A^k	Jacobian matrix in the k-direction
$C_{f1,2,3,4}$	coefficients in f
$\vec{C}^o, C^\pm$	coefficients in $\vec{W}^o, W^\pm$
C_T	thrust coefficient
c	sound celerity
$\vec{d}$	outflow direction
f	a non-linear function
$\bar{\bar{\mathsf{I}}}$	identity 3x3-matrix
K	a user-supplied factor
$k^{(2),(4)}$	coefficients in the scalar dissipation
L	matrix of left eigenvectors
$\vec{l}^o, l^\pm$	eigenvectors of $\mathcal{A}$
M	Mach-number
M_{TIP}	blade tip Mach-number
M_P	preconditioning matrix
$\dot{m}$	mass flux
$\vec{n}$	a unit vector
P, P_2	preconditioning suitable variables
p	pressure
p_t	total pressure
Q	change of variable for q
Q^*	solution of $f(Q) = 0$
$q = \|\|\vec{v}\|\|$	Euclidian norm of the velocity vector
q'	a normalising velocity
$\bar{q}$	limited velocity in the preconditioning
R	radius of rotors
Re	Reynolds-number
s	entropy
T	temperature
T_t	total temperature
V	primitive variables
$\vec{v}$	velocity vector
v_n	velocity component along $\vec{n}$
$\vec{v}_t$	velocity component normal to $\vec{n}$
W	characteristic variables
$\vec{W}^o, W^\pm$	$\lambda^{o,\pm}$-characteristic variables
z	alias in preconditioned eigenvalues

Greek characters:

α	incidence angle
α_f	exponent in f
α_{TPP}	incidence angle of the tip path plane
$\epsilon = \pm 1$	sign function
$\epsilon^{(2),(4)}$	factors in the scalar dissipation
Λ	matrix of eigenvalues
$\lambda^{o,\pm}$	eigenvalues of $\mathcal{A}$
μ	rotor advance ratio
ν	sensor function
ρ	density
θ	outlet flow angle
ξ	a relaxation parameter

Introduction

The German aerospace centre DLR has been involved from mid-1998 to end-2004 in the French-German cooperative project Complete Helicopter AdvaNced Computational Environment (CHANCE), which aimed at providing the French-German rotary wing industry with numerical tools able to simulate the flow around a fully equipped helicopter. The interested reader is refered to papers [6, 7] for an overview of the whole project.

In the frame of CHANCE activities, and among other work packages, DLR was committed to developing the actuator disc (AD) option in its proprietary flow solver FLOWer. A first study resulted in the selection of an appropriate numerical implementation of this feature, which was validated with the ONERA Dauphin configuration, see [4]. Second, the Chimera approach to computing fuselage/main rotor as actuator disc has been validated and presented in [1]. In a third step, this has been extended in [5] to the presence of the tail rotor modelled by an actuator disc too. This paper presents the final development of the quasi-steady approach, namely the simulation of engine exhausts by means of boundary conditions.

First, the derivation of boundary conditions for the simulation of engines is derived along with their preconditioned version for low-Mach number flows. Next, the configuration to be computed is presented and the demonstration computation is analysed and commented on.

Engine Boundary Conditions

Modelling the influence of an engine on the external flow-field can be done in considering only the inlet and outlet surfaces, on which physical boundary conditions are set. Engines are here assumed to run with both inlet and outlet fluid states in subsonic mode. Hence, following the one-dimensional theory of characteristics, one single variable is to be prescribed at engine inlet and four at outlet. A possible choice of quantities for the outlet surface is: total pressure p_t, total temperature T_t and the direction of the outflow $\vec{d}$, which all must be user-supplied. For the inlet surface use is made of the initially user-supplied static pressure p, which moreover can be iteratively adapted to reach mass flux balance between inflow and outflow.

A schematic engine is depicted in figure 1, where conventions for subscripts and unit normal vectors can be seen: i denotes the interior of the computational domain, b the boundary surface and BC the interior of the engine; also, the unit normal vector $\vec{n}$ on boundaries is always taken to point outwards of the computational domain, in this case inside the engine.

Engine boundary conditions are set after integration of a time-step from time t^n to time t^{n+1}. Hence, the fluid state referenced by the index i is to be understood as standing at time t^{n+1} too.

While deriving the characteristic variables use is made of a so-called linearising fluid state V_o and of an arbitrary unit vector $\vec{n}$. These two are assigned special values when applied to boundary conditions: the linearising fluid state is that in the first computational cell V_i next to the boundary and the unit vector stands orthogonally to the engine surface as described above.

Finally, let θ denote the angle between the ouflow direction $\vec{d}$ and the unit normal vector at outlet.

"Characteristic" Variables

The derivation of characteristic variables is briefly outlined for the sake of completeness and can be seen in full details in [10, 3]. The system of Euler equations in primitive variables reads:

$$\frac{\partial V}{\partial t} + A^k \frac{\partial V}{\partial x_k} = 0 \tag{1}$$

with the primitive variables, the contracted Jacobian matrix and an arbitrary unit vector respectively:

$$V = \begin{pmatrix} \rho \\ \vec{v} \\ p \end{pmatrix}, \qquad \mathcal{A} = n_k\, A^k, \qquad \vec{n} = \begin{pmatrix} n_x \\ n_y \\ n_z \end{pmatrix}. \tag{2}$$

The eigenvalues of system (1) are:

$$\begin{cases} \lambda^o = \vec{v} \cdot \vec{n} \\ \lambda^\epsilon = \vec{v} \cdot \vec{n} + \epsilon\, c \quad (\epsilon = \pm 1) \end{cases} \tag{3}$$

and grouped in the eigenvalue matrix:

$$\Lambda = \begin{pmatrix} \lambda^o \bar{\bar{\mathrm{I}}} & \vec{0} & \vec{0} \\ \vec{0}^t & \lambda^+ & 0 \\ \vec{0}^t & 0 & \lambda^- \end{pmatrix}. \tag{4}$$

A set of left eigenvectors of the matrix $\mathcal{A}$ is:

$$L = \begin{pmatrix} \vec{l}^o \\ l^+ \\ l^- \end{pmatrix} \tag{5}$$

or in expanded form

$$L = \begin{pmatrix} n_x & 0 & n_z & -n_y & -n_x/c^2 \\ n_y & -n_z & 0 & n_x & -n_y/c^2 \\ n_z & n_y & -n_x & 0 & -n_z/c^2 \\ 0 & n_x & n_y & n_z & 1/\rho c \\ 0 & -n_x & -n_y & -n_z & 1/\rho c \end{pmatrix}. \tag{6}$$

System (1) is then linearised about a given linearising fluid state V_o. That is, $\Lambda_o = \Lambda(V_o)$ and $L_o = L(V_o)$ are the eigenvalues and left eigenvectors of the matrix $\mathcal{A}_o = n_k A^k(V_o)$. Now, let the following expression

$$W(V) = L_o \cdot V \tag{7}$$

be refered to by the abused phrase of *characteristic variables*, which strictly speaking are addressable in three dimensions only using their differential. Equivalently, it holds:

$$W = \begin{pmatrix} \vec{W}^o \\ W^+ \\ W^- \end{pmatrix} = \begin{pmatrix} (\rho - p/c_o^2)\,\vec{n} + \vec{v} \times \vec{n} \\ p/\rho_o c_o + \vec{v} \cdot \vec{n} \\ p/\rho_o c_o - \vec{v} \cdot \vec{n} \end{pmatrix}, \tag{8}$$

or again more explicitely

$$W = \begin{pmatrix} (\rho - p/c_o^2)\, n_x + v\, n_z - w\, n_y \\ (\rho - p/c_o^2)\, n_y + w\, n_x - u\, n_z \\ (\rho - p/c_o^2)\, n_z + u\, n_y - v\, n_x \\ p/\rho_o c_o + u\, n_x + v\, n_y + w\, n_z \\ p/\rho_o c_o - u\, n_x - v\, n_y - w\, n_z \end{pmatrix}. \quad (9)$$

Engine Outlet

Since this is an engine outlet surface, the following holds

$$\vec{n} \cdot \vec{d}_{\text{BC}} = \cos\theta < 0 \quad (10)$$

and the sign of the eigenvalues is *a priori* known:

$$\lambda^o < 0, \qquad \lambda^+ > 0 \qquad \text{and} \qquad \lambda^- < 0. \quad (11)$$

As usual, characteristics approaching the boundary from the grid side cause the corresponding characteristic variables to be extrapolated from the computational domain onto the boundary surface. The set of boundary conditions is completed by one user-supplied quantity per remaining characteristic. Hence the complete set of conditions on the boundary reads:

$$\begin{cases} \text{physical conditions: } (\, p_t\,,\, T_t\,,\, \vec{d}\,)_b = (\, p_t\,,\, T_t\,,\, \vec{d}\,)_{\text{BC}}, \\ \text{numerical condition: } W_b^+ = W_i^+. \end{cases} \quad (12)$$

A first rewriting of the numerical condition leads to:

$$q_b \cos\theta + \frac{p_{t_{\text{BC}}}}{\rho_i c_i} \left(1 - q_b^2\, \frac{\gamma - 1}{2\gamma r T_{t_{\text{BC}}}}\right)^{\gamma/(\gamma-1)} = W_i^+ \quad (13)$$

where $q_b = ||\vec{v}_b||$ stands here for the L_2-norm of the velocity vector. A further reformulation of the previous equation leads to

$$f(Q) = \left(1 - Q^2\right)^{\alpha_f} + C_{f1}\, Q + C_{f2} = 0 \quad (14)$$

with

$$\begin{cases} \alpha_f = \gamma/(\gamma - 1) \\ q' = \sqrt{(2\gamma r T_{t_{\text{BC}}})/(\gamma - 1)} \\ Q = q_b/q' \\ C_{f1} = q'\, \cos\theta\, \rho_i c_i / p_{t_{\text{BC}}} \\ C_{f2} = -W_i^+\, \rho_i c_i / p_{t_{\text{BC}}} \end{cases}. \quad (15)$$

This non-linear equation in Q is solved *e.g.* via Newton iterations and, on compatibility grounds with the subsonic assumption, the solution Q^* must lie in the following interval

$$Q^* \;\in\; \left]\, 0; \sqrt{(\gamma - 1)/(\gamma + 1)}\, \right[. \quad (16)$$

The primitive variables on the boundary finally read:

$$\begin{cases} \rho_b = \left(p_{t_{\text{BC}}}/r T_{t_{\text{BC}}}\right)\, \left(1 - Q^{*2}\right)^{1/(\gamma-1)} \\ \vec{v}_b = Q^*\, q'\, \vec{d}_{\text{BC}} \\ p_b = p_{t_{\text{BC}}}\, \left(1 - Q^{*2}\right)^{\gamma/(\gamma-1)} \end{cases}. \quad (17)$$

Engine Inlet

Also in this case, the sign of the eigenvalues is *a priori* known:

$$\lambda^o > 0, \qquad \lambda^+ > 0 \qquad \text{and} \qquad \lambda^- < 0. \quad (18)$$

Then boundary conditions read:

$$\begin{cases} \text{physical condition:} \quad p_b = p_{\text{BC}}, \\ \text{numerical conditions: } W_b^+ = W_i^+ \quad \text{and} \quad \vec{W}_b^o = \vec{W}_i^o. \end{cases} \quad (19)$$

The numerical conditions can be expanded as:

$$\begin{cases} \left(\rho_b - p_b/c_i^2\right) \vec{n} + \vec{v}_b \times \vec{n} = \vec{W}_i^o \\ v_{n_b} + p_b/\rho_i c_i = W_i^+ \end{cases}, \quad (20)$$

and the primitive variables on the boundary easily follow:

$$\begin{cases} \rho_b = \;\; \vec{W}_i^o \cdot \vec{n} + p_{\text{BC}}/c_i^2 \\ \vec{v}_b = v_{n_b}\vec{n} + \vec{v}_{t_b} = \left(W_i^+ - p_{\text{BC}}/\rho_i c_i\right) \vec{n} + \vec{n} \times \vec{W}_i^o \\ p_b = \;\; p_{\text{BC}} \end{cases} \quad (21)$$

where $\vec{v}_t = \vec{v} - v_n \vec{n} = \vec{n} \times (\vec{v} \times \vec{n})$ is the velocity component normal to $\vec{n}$. Final re-arrangements yield:

$$\begin{cases} \rho_b = \rho_i + (p_{\text{BC}} - p_i)/c_i^2 \\ \vec{v}_b = \vec{v}_i - (p_{\text{BC}} - p_i)/\rho_i c_i\, \vec{n} \\ p_b = p_{\text{BC}} \end{cases}. \quad (22)$$

Mass Flux Coupling

The pressure at engine inlet is adjusted in accordance to the ratio of integrated mass fluxes at inlet and outlet:

$$p_{\text{IN}}^{\text{new}} = p_{\text{IN}}^{\text{old}} + \Delta p \quad (23)$$

with

$$\Delta p = \xi\, p_\infty \left(\frac{\dot{m}_{\text{IN}}}{\dot{m}_{\text{OUT}}} - 1\right) \quad (24)$$

where ξ is a relaxation parameter, $\dot{m}_{\text{IN}}$ and $\dot{m}_{\text{OUT}}$ are the integrated mass fluxes over the inlet and outlet surfaces of the engine.

Preconditioning

The low-velocity preconditioning implemented in FLOWer is that of Choi & Merkle [2]. First, the procedure is shortly outlined for the sake of completeness using the approach retained in [8], and the preconditioned boundary conditions are subsequently derived.

"Characteristic" Variables

The system of Euler equations is formulated in a set of variables P that makes the derivation easier, and the time derivative is multiplied on the left by the preconditioning matrix:

$$M_P^{-1}\, \frac{\partial P}{\partial t} + A_P^k\, \frac{\partial P}{\partial x_k} = 0 \quad (25)$$

with

$$P = \begin{pmatrix} p \\ \vec{v} \\ s \end{pmatrix}, \qquad ds = dp - c^2\, d\rho. \tag{26}$$

The preconditioning matrix of Choi & Merkle rewritten in P-variables reads

$$M_P^{-1} = \begin{pmatrix} c^2/\bar{q}^2 & \vec{0}^t & 1 \\ \vec{0} & \bar{\bar{\mathrm{I}}} & \vec{0} \\ 0 & \vec{0}^t & 1 \end{pmatrix} \tag{27}$$

where $\bar{q}$ is the limited velocity to prevent singularities

$$\bar{q}^2 = \min\Big(\max\big(K\, q_\infty^2\,,\, q^2\big)\,,\, c^2\Big), \tag{28}$$

K is a user-supplied parameter and the inverse matrix reads

$$M_P = \begin{pmatrix} \bar{q}^2/c^2 & \vec{0}^t & -\bar{q}^2/c^2 \\ \vec{0} & \bar{\bar{\mathrm{I}}} & \vec{0} \\ 0 & \vec{0}^t & 1 \end{pmatrix}. \tag{29}$$

Similarly, the eigenvalues and left eigenvectors of the resulting system are that of the contracted Jacobian matrix $\mathcal{A}_P = n_k M_P A_P^k$:

$$\begin{cases} \lambda^o = v_n \\ \lambda^\epsilon = \dfrac{1}{2}\left(v_n\, z + \epsilon\sqrt{v_n^2\, z^2 + 4\bar{q}^2(1 - v_n^2/c^2)}\right) \end{cases} \tag{30}$$

with

$$\epsilon = \pm 1 \qquad \text{and} \qquad z = 1 + \bar{q}^2/c^2. \tag{31}$$

A set of left eigenvectors for the system in P-variables is:

$$L = \begin{pmatrix} \vec{l}^o \\ l^+ \\ l^- \end{pmatrix} \tag{32}$$

with

$$(1 + v_n/\rho c^2)\, \vec{l}^o = \Big(\vec{0}\,;\, \bar{\bar{\mathrm{I}}} - \vec{n}\otimes\vec{n}\,;\, (1 + v_n/\rho c^2)\, \vec{n}\Big) \tag{33}$$

and

$$\bar{q}^2\, (\lambda^+ - \lambda^-)\, l^\epsilon = \Big(-1/\rho\,;\, -(v_n - \lambda^{-\epsilon})\, \vec{n}^t\,;\, v_n(v_n - \lambda^{-\epsilon})/\rho c^2\Big). \tag{34}$$

A transformation from variables P to the set of variables $P_2 = (p, \vec{v}, T)$ using $ds = -(\gamma - 1)\, dp + \gamma\rho\, dT$ and taking

$$W = L_o \cdot P_2 = \begin{pmatrix} \vec{W}^o \\ W^+ \\ W^- \end{pmatrix} \tag{35}$$

yields the characteristic variables:

$$\begin{cases} \vec{W}^o = \vec{C}_p^o\, p + C_q^o\, \vec{v}_t + \vec{C}_T^o\, T \\ W^\epsilon = C_p^\epsilon\, p + C_q^\epsilon\, v_n + C_T^\epsilon\, T \end{cases} \tag{36}$$

with the following expressions for the $\vec{W}^o$-coefficients

$$\begin{cases} \vec{C}_p^o = -(\gamma - 1)\, \vec{n} \\ C_q^o = 1/(1 + v_{n_o}/\rho_o c_o^2) \\ \vec{C}_T^o = \gamma\rho_o\, \vec{n} \end{cases} \tag{37}$$

and for the W^ϵ-coefficients

$$\begin{cases} C^\epsilon = \bar{q}_o^2\, (\lambda_o^+ - \lambda_o^-) \\ C^\epsilon \cdot C_p^\epsilon = -\epsilon\left(1 + v_{n_o}(v_{n_o} - \lambda_o^{-\epsilon})\, (\gamma - 1)/c_o^2\right)/\rho_o \\ C^\epsilon \cdot C_q^\epsilon = -\epsilon\left(v_{n_o} - \lambda_o^{-\epsilon}\right) \\ C^\epsilon \cdot C_T^\epsilon = \epsilon\, v_{n_o}\left(v_{n_o} - \lambda_o^{-\epsilon}\right)\gamma/c_o^2 \end{cases} \tag{38}$$

where the subscript o indicates that they are all functions of the linearising state.

Engine Outlet

Since the procedure used here is identical to the one in the non-preconditioned case, only differences are reported. The numerical boundary condition reads:

$$W_b^+ = W_i^+ \tag{39}$$

which can be rewritten as

$$C_p^+\, p_b + C_q^+\, q_b\, \cos\theta + C_T^+\, T_b = W_i^+ \tag{40}$$

or also equivalently

$$f(Q) = C_{f1}\,(1 - Q^2)^{\alpha_f} + C_{f2}\, Q + C_{f3}\,(1 - Q^2) + C_{f4} = 0 \tag{41}$$

with

$$\begin{cases} \alpha_f = \gamma/(\gamma - 1) \\ q' = \sqrt{2\gamma r T_{t_{\mathsf{BC}}}/(\gamma - 1)} \\ Q = q/q' \\ C_{f1} = C_p^+\, p_{t_{\mathsf{BC}}} \\ C_{f2} = C_q^+\, q'\cos\theta \\ C_{f3} = C_T^+\, T_{t_{\mathsf{BC}}} \\ C_{f4} = -W_i^+ \end{cases}. \tag{42}$$

And primitive variables are calculated exactly as in equation (17).

Engine Inlet

Alike before the numerical boundary conditions read:

$$W_b^+ = W_i^+ \qquad \text{and} \qquad \vec{W}_b^o = \vec{W}_i^o, \tag{43}$$

which leads to

$$\begin{cases} p_b = p_{\mathsf{BC}} \\ T_b = T_i + (p_{\mathsf{BC}} - p_i)\, (\gamma - 1)/\gamma\rho_i \\ \vec{v}_b = \vec{v}_i - (p_{\mathsf{BC}} - p_i)/\rho_i(v_{n_i} - \lambda_i^-)\, \vec{n} \end{cases}. \tag{44}$$

Scheme Adaption

The configuration studied in this paper has been run with the usual central scheme by Jameson with

scalar dissipation along with low-velocity preconditioning. Unfortunately, severe unphysical aspects showed up in the flow solution and necessitated an adaption of the numerical scheme for the convection terms.

First, small and very localised regions of very hot gases have been observed to develop at approximately 1.7 nozzle diameter downstream of the engine outlet surfaces. Independently of any attempt to tune the scheme parameters, these spots remained stationary and all the more distinguishable as the temperature increased about 115% with respect to the exhaust temperature... Increasing the latter to its nominal value was even impossible, since the code invariably crashed with negative densities.

Second and conversely, the temperature distribution on the fuselage surface exhibited unsatisfactory cold spots around the engine exhausts that proved stationary too.

By means of a model hot plume configuration, the problem origin could be traced back to the discretisation scheme for the convection fluxes, an adaption of which is suggested below.

A Possible Workaround The artificial dissipation flux of the Jameson scheme is made of a blend of first and third differences of $(\rho, \rho\vec{v}, \rho H)$-variables. Blending is tuned by means of two coefficients, one in front of the first difference

$$\epsilon^{(2)}_{i+\frac{1}{2}} = k^{(2)} \max\Big(\nu_{Pi}\,,\,\nu_{Pi+1}\Big) \tag{45}$$

and the other one in front of the third difference

$$\epsilon^{(4)}_{i+\frac{1}{2}} = \max\Big(0\,,\,k^{(4)} - \epsilon^{(2)}_{i+\frac{1}{2}}\Big) \tag{46}$$

where the index $i+1/2$ refers to the cell face between cells with indices i and $i+1$. How large both coefficients are relative to each other is managed, apart from $k^{(2)}$ and $k^{(4)}$, by a pressure sensor

$$\nu_{Pi} = \left|\frac{p_{i+1} - 2\,p_i + p_{i-1}}{p_{i+1} + 2\,p_i + p_{i-1}}\right| \tag{47}$$

assuming values between 0 (smooth regions) and 1 (strong pressure gradients at shocks). Should the pressure sensor increase, the coefficient $\epsilon^{(4)}$ is reset to 0, thus switching off the third difference term and causing the scheme to reduce to first order spatial accuracy. This is the usual way to get solver robustness and a wiggle-free solution at shocks.

The idea is now to use the same trick at strong temperature gradients using a temperature sensor

$$\nu_{Ti} = \left|\frac{T_{i+1} - 2\,T_i + T_{i-1}}{T_{i+1} + 2\,T_i + T_{i-1}}\right| \tag{48}$$

and adding it into the max-function used in $\epsilon^{(2)}$

$$\epsilon^{(2)}_{i+\frac{1}{2}} = k^{(2)} \max\Big(\nu_{Pi}\,,\,\nu_{Pi+1}\,,\,\nu_{Ti}\,,\,\nu_{Ti+1}\Big) \tag{49}$$

hence hopefully not disturbing smooth solution areas.

This modification allowed the exhaust temperature to be raised to its originally specified value and the computation to be carried on. The surface temperature distribution is now free of any cold spot and the hot gas plumes exhibit only a temperature increase of 16% that, although still unsatisfactory, makes the simulation possible.

Results

The Configuration

The configuration under consideration is that of the EC-145 consisting of the fuselage, both main and tail rotors modelled by actuator discs and the engines modelled by boundary conditions at their inlet and outlet surfaces.

The helicopter experiences a high-speed forward flight with the following flight conditions:

$$M_\infty = 0.21, \quad \alpha = 0^o, \quad \mathrm{Re}_\infty = 4.33\,10^6\ (\mathrm{m}^{-1}), \tag{50}$$

where the angle α is measured between the incident velocity and the floor of the cell. Global parameters for the main actuator disc are:

$$\begin{gathered} C_T = 0.0077, \quad M_{\text{TIP}} = 0.64, \quad R = 5.5\ (\mathrm{m}), \\ \mu = 0.33 \quad \text{and} \quad \alpha_{\text{TPP}} = -5^o, \end{gathered} \tag{51}$$

which are those of the ATR-A rotor running with the aforementioned incident Mach-number and where α_{TPP} is the incidence of the flow with respect to the tip path plane. The force distribution applied on the surface of the actuator disc has been previously computed with FLOWer for the trimmed isolated rotor. As for the tail actuator disc, global parameters are

$$C_T = 0.0089, \quad M_{\text{TIP}} = 0.64, \quad R = 0.97\ (\mathrm{m}) \tag{52}$$

that allow deriving a constant pressure jump modelling of the corresponding rotor. In figure 2 are depicted three-dimensional force vectors for each discretisation point of both actuator disc surfaces; the colouring variable is the force component normal to each disc respectively.

As a result of combining separately trimmed elements and since a global trim procedure has not been implemented up to now, it is to be noted that the complete configuration itself is not trimmed.

The surface discretisation of both inlet and outlet engine surfaces is to be seen in figure 3, for which the set of outlet nominal quantities is

$$\begin{gathered} \frac{p_t}{p_\infty} = 1.013, \quad \frac{T_t}{T_{t\,\infty}} = 2.546, \\ \vec{d} = \big(0.98\,,\,-0.14\,,\,\pm 0.14\big) \end{gathered} \tag{53}$$

where the total pressure and total temperature have been normalised by the static pressure and total temperature at infinity respectively. The outlet directions $\vec{d}$ are such that each engine exhausts away from the tail boom in the z-direction.

The complete system has been assembled and computed using the Chimera technique (please refer to [5] for details) and a slice of the grid system in the symmetry plane is displayed in figure 4.

Discussion

Combining the different modelling possibilities yields four different runs: (a) fuselage alone (not reported on), (b) fuselage with engine plume simulation, (c) fuselage with rotor simulation using actuator discs and (d) fuselage with engines and actuator discs.

Once the computation stabilised, the engines ended up in the following running states:

	p_{inlet}	mass flux
left engine	1.0136	$7.97\ 10^{-3}$
right engine	1.0153	$8.59\ 10^{-3}$

in non-dimensional form.

In figure 5 is depicted, for run (d), the surface distribution of the pressure coefficient along with friction lines in the vicinity of the inlet and outlet engine surfaces. Solely on the inlet surfaces, the normal component of the velocity vector is to be seen, thought of as representative of the inlet mass flux. Flow characteristics on both the left and right sides are identical; therefore only the left one is shown and commented on.

By construction of the present boundary conditions, the engine intake operates with a constant specified pressure over its entire surface (here 1.0136). The pattern of friction lines reveals a lower pressure on the nose (1.0109–1.0127), just in front of the intake, and a higher one on the very top portion of the nose (1.0176–1.0221). In fact, the fluid in the boundary layer in front of the engine has not enough energy to withstand the overpressure of the intake and is deflected sidewards. In the same time, due to the higher pressure of the stagnation point located on the "nose eyebrow", the boundary layer fluid can enter the intake. At engine outlet, a complicated surface flow pattern with many point and line singularities results from the combination of the exhaust jet (see bottom sub-picture of figure 8) with the flow separation region on the rear of the cell (see bottom sub-picture of figure 7).

How the hot gas plume evolves as it is convected downstream in case of run (d) can be explained with picture 6 where the field distribution of the temperature and of the x-component of the vorticity vector is to be seen. Again, because of similar features on both sides, only the left one is reported on.

Initially, the cross-section of the hot gas plume assumes the one of the engine nozzle, that is approximately circular. Now, because of the jet being exhausted to the left (see the components of the outflow direction in equation set 53) and because of the surrounding fluid flowing to the right (due to the shape of the engine casing and of the cell), x-vorticity arises at the top-right and at the bottom left of the jet rim. In a first section, from the engine nozzle down to the junction of the cell with the tail boom, the aforementioned vorticity tends to strip off hot gases from the jet core. In a second section, from the cell/tail boom junction down to the horizontal stabiliser, the strong vortex originating from the large flow separation on the cell rear comes into play along with its companion contra-rotating vortex that stems from the top fore part of the tail boom. From these two, only the first one plays a role in the rolling up of the hot gas plume, since the other one lies too far away above. (By the way, this is not the case on the right side where both vortices deform the jet.) Third, the jet is sliced by the horizontal stabiliser, which actually generates very little deformation. In a fourth part, the downwash of the tail actuator disc makes the whole system drift leftwards without major shape modification. (Again, it is to be noted on the right side that the transformation of the upper portion of the jet cross-section into almost a triangle is due to the combined action of vortices generated directly behind the bottom part of the fin and of the suction effect of the tail actuator disc.)

In comparing both runs (b) and (d), it is possible to assess the influence of the downwash of both actuator discs on the flow separation on the rear of the cell (figure 7) and on the hot gas plume (figure 8). Each figure is subdivided in two sub-pictures: run (b) on the top and run (d) on the bottom.

For each sub-picture in figure 7 are depicted friction lines of the corresponding run and also in dashed lines, for comparison purposes, the salient features of the other one. These can be singular lines or singular points of attractive (converging lines) or repulsive (diverging lines) type. Note also that converging points can look either like cross wires or like a spiral. The flow solution with the actuator discs exhibits, as general trend, a shift towards the left of the complete pattern: to be noticed are the diverging lines on the bottom of the tail boom, in the middle of the boot and the line defining the separation bubble. But more important is the relatively large shift of the spiral converging point on the right side, which is the origin of the strong vortex on that side.

In figure 8 is displayed the temperature distribution on the helicopter surface and also as a three-dimensional contour for the value $T = 1.19$. As expected, the plume pattern of run (b) turns out to be relatively symmetrical with respect to the plane $z = 0$ in comparison to that of run (d). This results in the presence of one hot spot on each horizontal stabiliser for run (b), whereas only one shows up on the left stabiliser for run (d), which correlates with the right side of the bottom sub-picture of figure 6 where it is seen that the stabiliser slices the hot gas plume just in its colder middle. This matter of fact is a pure consequence of the flight conditions and of the rotor run parameters.

Comparisons between run (c) and (d) are drawn looking at the distribution of the pressure coefficient and of the temperature on the top centre-line (figure 9)

and on a section of the left horizontal stabiliser close the tail boom (figure 10).

First on figure 9, the temperature does not incur any modification down to the cell/tail boom junction where a mild 6% increase takes place, and is then stabilised around 3% increase down to the fin. (Note that, without heat addition, the static temperature is equal to the stagnation temperature on the fuselage, and thus yields a floor value higher than unity.) As for the pressure, only slight changes are to be noted: first in the region of the engine intakes, where fluid is now (run d) ingested thus modifying the flow pattern, and second in the fore part of the tail boom.

On figure 10 is to be noted the temperature increase between 8% and 14% where the lower side remains hotter than the upper one and this can also be inferred from picture 6. From the pressure distribution for run (c) (dashed line) it can be seen that the exerted force on the present section is directed to the bottom (negative lift), which is the expected stabilising role of the horizontal stabiliser in cruise forward-flight. On the contrary, this is not obvious any longer for run (d) (solid line) where the zones of positive lift (front part) and negative lift (rear part) have increased and decreased respectively. Here, hot air seems to reduce the magnitude of the sectional negative lift.

Conclusion

Concluding the series of developments for quasi-steady computations of complete helicopter configurations in the frame of the CHANCE programme, the simulation of engine exhausts has been modelled using boundary conditions at inlet and outlet, the numerics of which has been first derived. The one-dimensional theory of characteristics has been specialised to inflow and outflow conditions and a preconditioned version for low-velocities has been presented. Additionally, a modification of the scalar artificial dissipation using a temperature sensor has increased the scheme robustness at high temperature gradients.

Next, a demonstration computation has been carried out on the EC-145 helicopter configuration. The discussion of the results showed that the hot gas plumes are heavily stretched and distorted by the various vortical systems that they come across. A first zone of vorticity generated at the jet rim initiates the stretching from the engine nozzle down to the cell/tail boom junction. Subsequently, both the strong vortex from the separation bubble on the cell boot and its companion contra-rotating vortex from the tail boom carry on the deformation down to the horizontal stabilisers. Then after having been traversed by the stabilisers, the exhausts gases experience the downwash of the tail actuator disc and undergo a final deformation due to vortices emitted on the rear side of the fin.

The effect of the downwash of mainly the main actuator disc has been evidenced by means of the separation area behind the cell. The complete pattern of singular lines and points exhibit a shift to the left including the origin points of the strong vortices. Additionally, only one hot spot on the left horizontal stabiliser shows up instead of one on each stabiliser.

The inclusion of hot gases has been shown to have only minor effects on the pressure distribution on the top centre-line, whereas the temperature distribution experiences an increase along the tail boom. Finally, a cross-section of the left horizontal stabiliser at the location of the hot spot showed that hot gases can reduce the magnitude of the negative lift. Thus it appears that an aerodynamic analysis of the rear control surfaces of an helicopter must include the hot gas plumes of the engines.

Acknowledgements

This work has been carried out under financial support of the German ministry BMWA with contract number 20H0303B. The author acknowledges gratefully the help of Alessandro d'Alascio of Eurocopter Deutschland who provided the grid for the fuselage of the EC-145, data for both actuator discs and a data set for the engine plume simulation.

References

[1] **A. D'Alascio, A. Berthe, F. Le Chuiton**, *Application of CFD to the fuselage aerodynamics of the EC-145 helicopter. Prediction of unsteady phenomena and of the time-averaged influence of the main rotor*, 29th European Rotorcraft Forum, Friedrichshafen, Germany, September 2003

[2] **Y.-H. Choi, C.L. Merkle**, *The application of preconditioning to viscous flows*, Journal of Computational Physics, 105 (1993), 207-223

[3] **C. Hirsch**, *Numerical Computation of Internal and External Flows, Volume 2, Computation Methods for Inviscid and Viscous Flows*, John Wiley & Sons, 1990

[4] **F. Le Chuiton**, *Actuator disc modelling for helicopter rotors*, Aerospace Science and Technology, 8 (2004), 285-297

[5] **F. Le Chuiton**, *Chimera simulation of a complete helicopter with rotors as actuator discs*, Notes on Numerical Fluid Mechanics and Multidisciplinary Design, Springer Verlag, 2005 (accepted contribution)

[6] **M. Costes, K. Pahlke, A. D'Alascio, C. Castellin, A. Altmikus**, *Overview of results obtained during the 6-year French-German CHANCE project*, AHS Forum 61, Grapevine (TX), June 1-3, 2005

[7] **K. Pahlke, M. Costes, A. D'Alascio, C. Castellin, A. Altmikus**, *The 6-year French-German CHANCE project*, 31st European Rotorcraft Forum, Florence, Italy, September 2005

[8] **R. Radespiel, E. Turkel, N. Kroll**, *Assessment of Preconditioning Methods*, DLR Forschungsbericht 95-29, 1995

[9] **R. Schweikhard, F. Le Chuiton**, *Actuator disc for helicopter rotors in the unstructured flow solver TAU*, 31st European Rotorcraft Forum, Florence, Italy, September 2005

[10] **D. L. Whitfield, J. M. Janus**, *Three-dimensional unsteady Euler equations solution using flux vector splitting*, AIAA 17th Fluid Dynamics, Plasma Dynamics and Lasers Conference, June 1984, Snowmass, Colorado

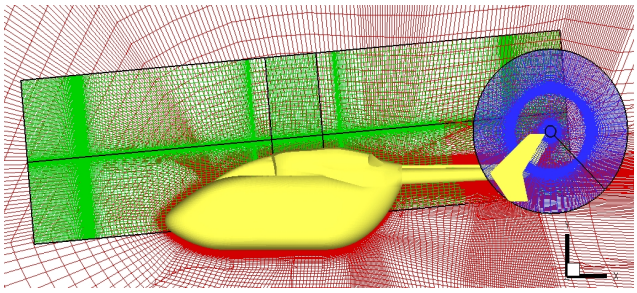

Figure 4: Grid system of the EC-145 in the symmetry plane.

Figures

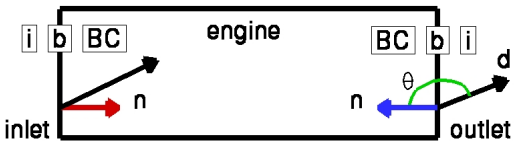

Figure 1: Engine sketch

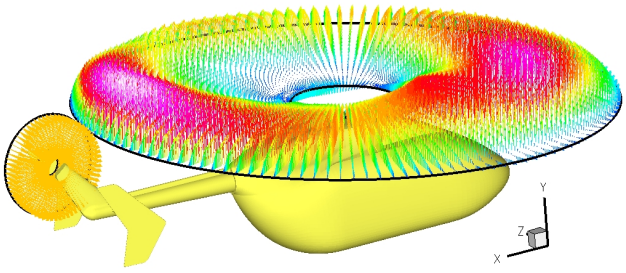

Figure 2: Source terms on the main and tail rotors with a force distribution and a constant pressure jump respectively.

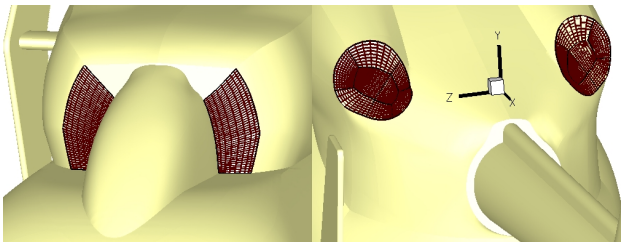

Figure 3: Discretisation of the inlet and outlet engine surfaces.

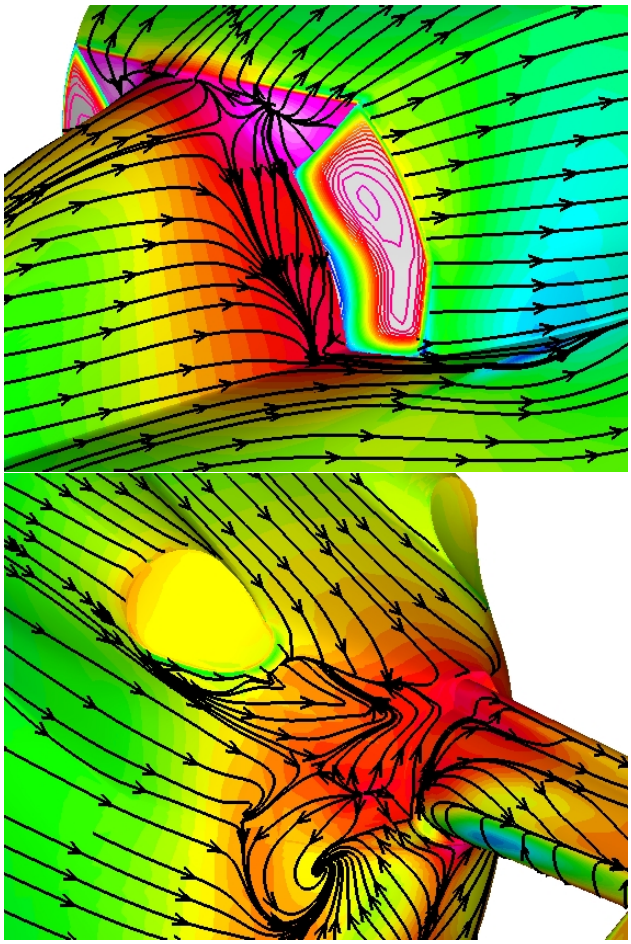

Figure 5: Engine inlet (top) and outlet (bottom) surfaces of the complete configuration (run d). Friction lines and surface distribution of the pressure coefficient except on inlet surfaces where the normal velocity component is displayed.

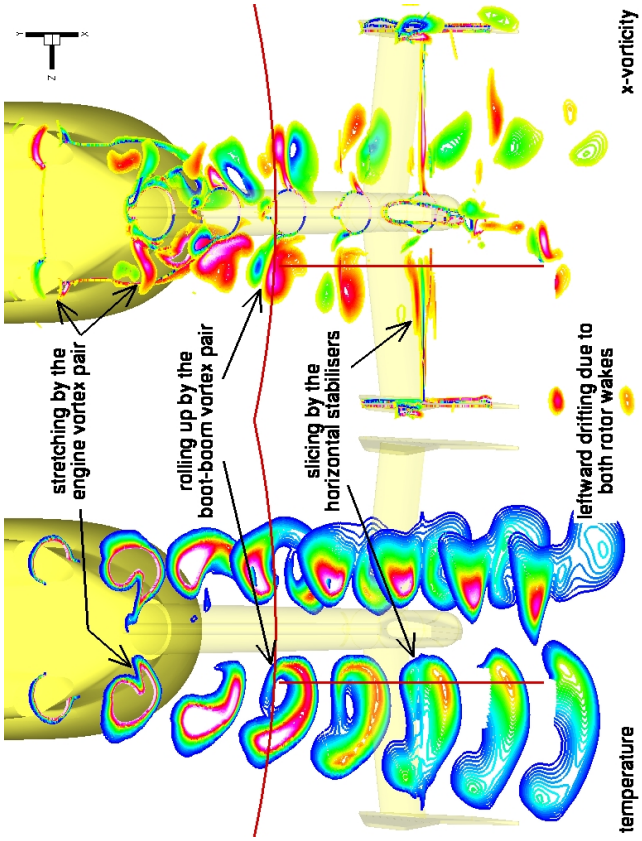

Figure 6: Field distribution of the temperature (bottom) and of the x-component of the vorticity vector (top) of the complete configuration (run d).

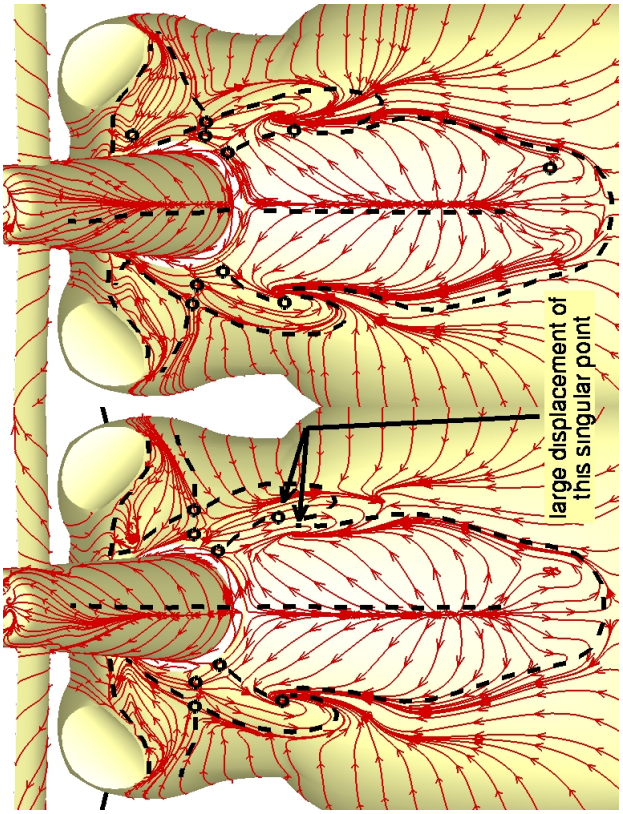

Figure 7: Friction lines: with both main and tail actuator discs (bottom, run d) and without (top, run b). For each sub-picture, the salient features of the other case are overlaid with dashed lines.

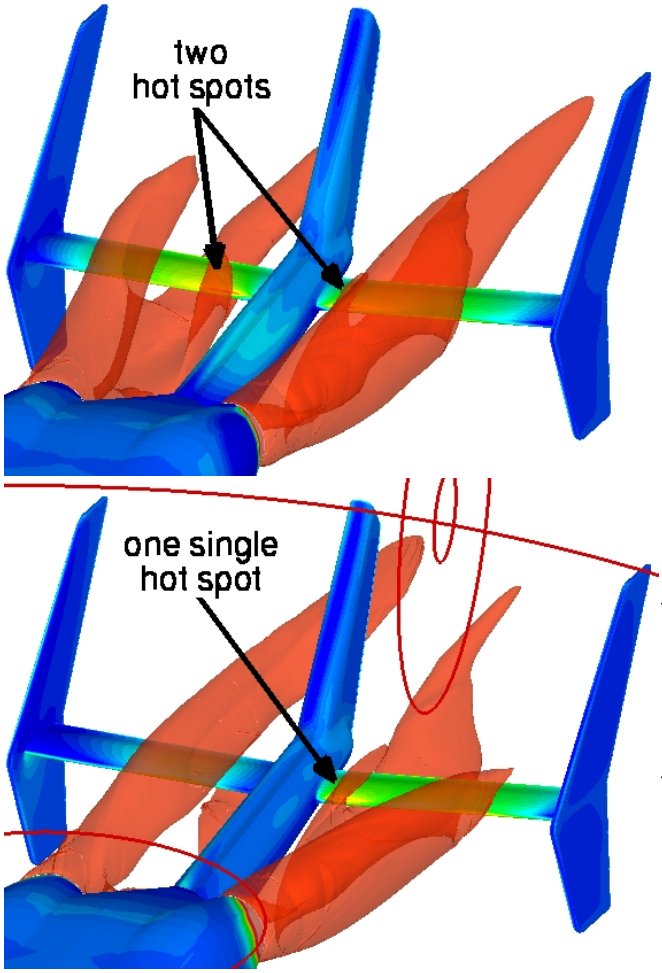

Figure 8: Three-dimensional and surface temperature contours; with both main and tail actuator discs (bottom, run d) and without (top, run b).

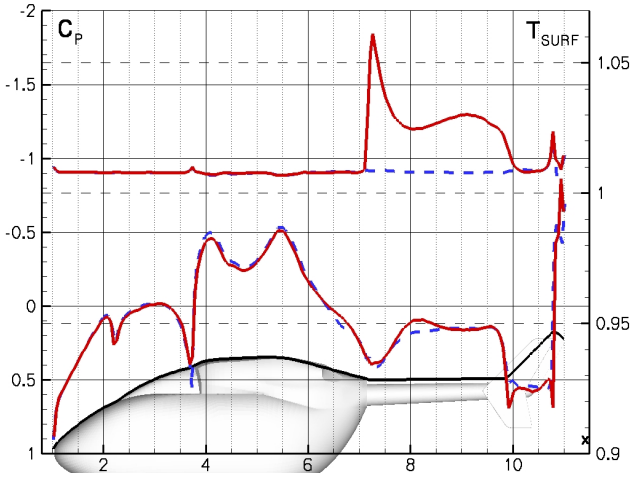

Figure 9: Distribution of the pressure coefficient and of the surface temperature on the top centre line with engine plume simulation (solid, run d) and without (dashed, run c).

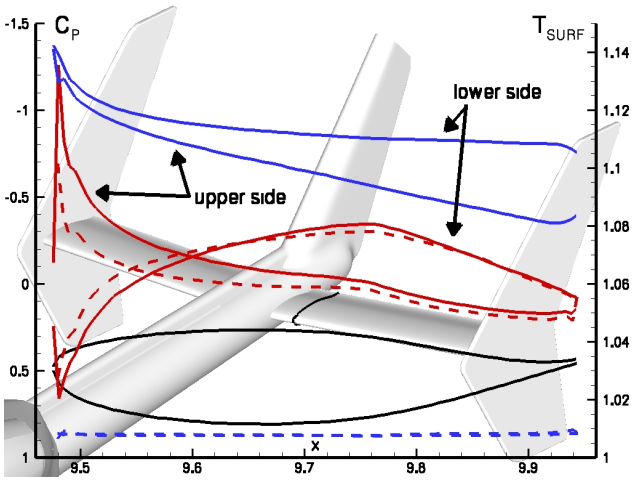

Figure 10: Profiles for the pressure coefficient and temperature distribution on a section near the root of the left horizontal stabilizer: with engine plume simulation (solid, run d) and without (dashed, run c).